ADVANCED FUNCTIONAL MATERIALS
www.afm-journal.de

Time-Resolved Control of MOF-Nanoparticle Heterojunctions for Crystal Composites with Tailorable Photocatalytic Performance

Carmen Fernández-Conde, Horatiu Szalad, Neyvis Almora-Barrios, Antonio Ribera, Josep Albero, and Carlos Martí-Gastaldo**

The structural and compositional diversification of Metal-Organic Frameworks (MOFs) continues to grow, along with the opportunities they offer in H_2 photoevolution or CO_2 photoreduction. This often requires the use of metal co-catalysts for improving the efficiency and selectivity of the reaction. However, most studies often overlook how the integration of these two components can be used to tailor the photocatalytic performance of a given framework. Taking advantage of a new synthetic methodology that allows the growth of titanium-based MUV-10 crystals through continuous injection of its components, here it is demonstrated how the time-resolved injection of Pt nanoparticles (NPs) at different stages of crystal growth results in tunable MOF/Pt heterojunctions with varying photocatalytic efficiencies, which can be used to boost performance by up to 2.5 times depending on the injection time.

1. Introduction

The design and modification of Metal-Organic Frameworks (MOFs),[1] as well as their increasing applications in separation, storage, catalysis, sensing, electronic/ionic conduction or biomedical applications,[2] have highlighted both their limitations and advantages compared to other families of porous materials. The design of photocatalytic MOFs, either by integrating homogeneous catalysts into their porous structures or by tailoring their organic and inorganic components to combine high surface areas with intrinsic photoactivity, is a good example of the distinctive possibilities offered by this family of materials for the hydrogen evolution reaction, CO_2 photoreduction, or dye degradation.[3–5] In this context, titanium (IV) MOFs are arguably the most suitable candidates because of their good chemical and thermal stability, low toxicity, natural abundance (ninth most abundant element in the Earth's crust), and photoredox properties. Although the high reactivity of Ti^{4+} in solution makes the synthesis of crystalline frameworks difficult compared to other highly charged metals such as Zr^{4+},[6,7] recent years have witnessed an increasing diversification in the structure, surface area, composition, and tunable light absorption of this family of MOFs.[8] Although classical semiconductor concepts are often used to analyze photocatalytic activity,[9] the metal-organic nature of these materials restricts the photoexcitation and linker to metal charge separation phenomena to the molecular nodes, which often results in a periodic distribution of homogeneous photocatalysts with reduced charge carrier mobility for limited performance. Despite this fundamental difference, strategies developed for semiconductors as their integration with conducting polymers[10] or the formation of heterojunctions,[11] are often used to minimize the spontaneous recombination of holes and electrons and increase the activity of a given photocatalyst.

Heterojunctions in MOFs are based on the integration of the framework with metal oxides,[12] g-C_3N_4,[13] or even another MOF (MOF-on-MOF)[14,15] to facilitate charge-carrier migration at the interface generated between the two components and facilitate the migration of holes and electrons to the respective reduction and oxidation sites, thus improving the overall photocatalytic performance. These heterojunctions can be prepared by solvothermal synthesis, impregnation, and electro- or photodeposition,[16] methods that are focused on activity enhancement but do not grant control over the hierarchical integration of both components at the crystal level or permit tailoring their electronic hybridization at the interface, both relevant to engineer the performance of the resulting heterojunctions.

C. Fernández-Conde, N. Almora-Barrios, C. Martí-Gastaldo
Functional Inorganic Materials Team (Funimat)
Instituto de Ciencia Molecular (ICMoL)
University of Valencia
C/ Catedrático José Beltrán Martínez, 2, Paterna 46980, Spain
E-mail: carlos.marti@uv.es
H. Szalad, J. Albero
Instituto Universitario de Tecnología Química UPV-CSIC
Polytechnic University of Valencia-Council Superior of Scientific Research
Avenida de los Naranjos s/n, Valencia 46022, Spain
E-mail: joalsan6@itq.upv.es
N. Almora-Barrios
Departamento de Química Física
University of Valencia Carrer
del Doctor Moliner, 50, Burjassot 46100, Spain
A. Ribera
Departamento de Química Inorgánica
University of Valencia Carrer
del Doctor Moliner, 50, Burjassot 46100, Spain
The ORCID identification number(s) for the author(s) of this article can be found under https://doi.org/10.1002/adfm.202425851

DOI: 10.1002/adfm.202425851

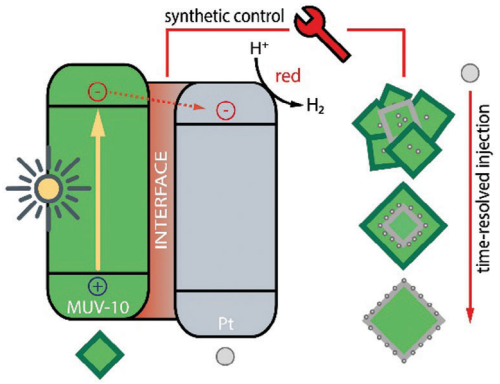

Figure 1. Time-resolved injection of platinum nanoparticles during MOF crystal formation as a synthetic tool to exert control over the interface of Pt/MOF heterojunctions for varying photocatalytic performance.

Although the molecular nature and periodic structure of MOFs offer tools for improved structural and electronic integration by matching the chemistry and symmetry of the crystal surface with the additional component, to the best of our knowledge, no previous work has addressed this possibility. Taking advantage of the compatibility of the titanium-based MUV-10 crystals with a dynamic synthesis method that enables the injection of additional components during its nucleation,[17] here we demonstrate how the time-resolved incorporation of Pt nanoparticles (NPs) can modify their integration and hybridization in the corresponding Pt@MUV-10 crystal composites to enable the formation of tailorable heterojunctions that can enhance the photogeneration of H_2 by up to 2.5 times depending on the time at which the co-catalyst is injected (**Figure 1**).

2. Results and Discussion

Monodisperse platinum nanoparticles of near to 3 nm in size (**Figure 2a**) were prepared according to the reported reduction methods and characterized with TEM, UV-Vis spectroscopy and dynamic light scattering (Section S2.1.1, Supporting Information). Pt@MUV-10 crystals were synthesized by using a triple syringe pump system that allows the injection of three stock solutions into a round bottom flask preheated at 120 °C under inert atmosphere and constant stirring. As shown in Figure 2b, two channels continuously inject stock solutions of the MOF molecular precursors, $CaCl_2$ and $Ti(O^iPr_4)$ dissolved in a mixture of DMF and acetic acid and the linker (H_3BTC = benzene-1,3,5-tricarboxylic acid) dissolved in DMF, Ar bubbled to preserve the moisture-free conditions and avoid the formation of titanium oxides. As we have shown previously,[17] adjusting the feed rates under supersaturation conditions enables the formation of homogeneously sized MUV-10 crystals with characteristics equiv. to those obtained by the more conventional solvothermal method.[8c] The availability of a third channel allows the time-resolved injection of an additional component. We used it for spot injections of 1 mL of Pt nanoparticles in MeOH (1.33 mM) at times $t_1 = 0$, $t_2 = 27$, and $t_3 = 105$ min, that correspond to early (e), intermediate (i) and late (l) stages of MUV-10 nucleation and growth for the formation of the corresponding Pt@MUV-10(e), (i), and (l) crystal composites (Figure 2c). All synthetic details are summarized in the Supporting Information (Section S2.2, Supporting Information). NPs with sizes well above the diameter of the 3D channels of MUV-10 (1 nm) were intentionally chosen to exclude physisorption in the open framework, forcing instead their integration into the solid during MOF assembly.

SEM images confirm the formation of crystals in all three cases, with clear differences in size and morphology depending on the time of Pt injection (Figure 2d). Compared to Pt@MUV-10(l) which shows octahedral crystals with well-defined edges and micrometer sizes, the crystals in (i) and (e) are smaller, with rounded edges and more polydisperse in size. These differences do not imply phase segregation or compositional changes and agree well with the MUV-10 composites prepared under similar conditions by injection of Au.[8c] All samples present the same relative proportion of Ti and Ca consistent with the formation of the Ti_2Ca_2 heterobimetallic cluster, with a slight excess of titanium possibly associated with the formation of a small proportion of amorphous oxide in all cases. In turn, ICP-MS analysis shows a linear decrease in the amount of Pt incorporated, that ranges from a maximum of 2150 ppm in Pt@MUV-10(e) to a minimum of 1050 ppm in (l) for near to 50% less (Figure 2e). This decrease in Pt for later injection times suggests a dependence with the stage of MUV-10 formation. While for an early stage of nucleation, the NPs can be easily incorporated, this incorporation would be limited as crystal formation progresses. To confirm whether this effect is general or dependent on the volume of Pt NPs injected, we conducted injection experiments with varying volumes of 1, 5, and 10 mL for the three injection times. The results confirm that the highest incorporation always occurs for the early nucleation stage regardless of the volume injected. However, triplicate analysis of the samples suggests greater dispersion in the concentration of incorporated Pt as the injected volume increases (Figure S18, Supporting Information).

These relative differences are also visible from the color change of the solids, which gradually pale for lower Pt concentrations. This color change does not correlate linearly with the modification of the optical band gap of the solids (Figure S6 and Table S3, Supporting Information). While the composites (e) and (l), with the highest and lowest net incorporation of Pt, exhibit band gap values of 3.31 and 3.40 eV, respectively, which are very similar to the 3.53 eV of bare MUV-10, composite (i) shows a much more pronounced reduction into the visible region (2.69 eV) which does not directly correspond to the concentration of incorporated Pt and suggests an additional effect exclusive to this composite. Powder X-ray diffraction and N_2 adsorption isotherms of Pt@MUV-10(e), (i) and (l) confirm the formation of the MUV-10 structure with minimal deviations in surface area and pore size of the composites compared to the pristine material (Figure 2f–h). The cell parameters obtained by LeBail refinement of all composites (Section S2.2.1 and Table S5, Supporting Information) are also consistent with the formation of the framework with negligible structural changes.

According to these results, the addition of nanoparticles at varying times causes clear changes in crystal size and effective Pt loading, suggesting a direct effect on MOF assembly, the changes that this time-resolved injection might have in controlling the spatial distribution and electronic hybridization of the nanoparticles within the crystal are arguably more important to account

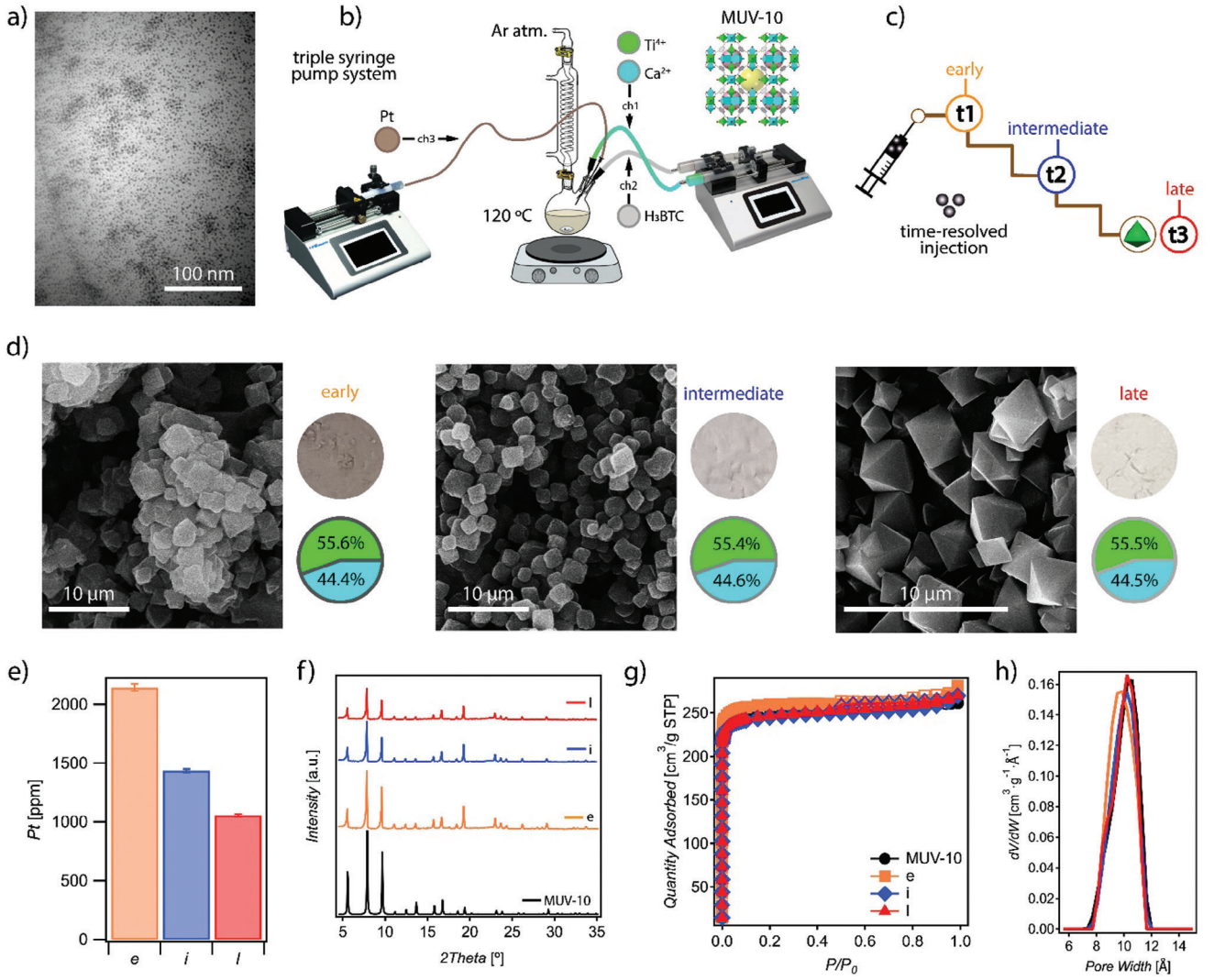

Figure 2. a) TEM image of Pt nanoparticles. b) Triple syringe pump system used to prepare Pt@MUV-10 crystal composites by c) time-resolved injection of a methanol solution of Pt nanoparticles at an early (e), intermediate (i) and late (l) stage of MUV-10 growth. d) SEM images of Pt@MUV-10(e), (i) and (l) show the formation of crystals with varying size that display the expected Ti:Ca ratio. e) ICP-MS confirms a reduction in Pt concentration as nanoparticle injection is delayed with small statistical deviations calculated for three alternative experiments. f) PXRD patterns confirm the formation of MUV-10 frameworks in all cases. g) N_2 adsorption isotherms at 77 K and h) experimental pore size distributions compared to the pristine MOF.

for effective changes in the resulting heterojunctions. TEM analysis confirms the formation of particles with well-defined edges, but the low transmissivity of the crystals did not allow to visualize with clarity the relative position of the NPs within them (Figure S10, Supporting Information). We used FIB-SEM to solve this problem. The samples were prepared by embedding a few µg into an innocuous polymer resin (Figure S12, Supporting Information). According to our experience,[18,19] this treatment prevents molecular crystals from collapsing during the ion beam treatment. The images confirm the presence of Pt NPs in all cases but with different distributions (**Figure 3**a). Pt@MUV-10(e) shows a high density in the crystal core compared to (l) which shows a lower density. The images confirm what was anticipated by ICP analysis, while early addition (e) seems to favor Pt loading upon later crystallization, late addition to an already formed crystal (l) hinders its incorporation and restricts it to the outer surface of the crystals. Pt@MUV-10(i) shows a different behavior. The nanoparticles are incorporated into inner sections of the crystal but show an organized distribution that is not present in (e) or (l). Our experiments with methanol injections as blank experiments in the absence of Pt confirm that this pattern is not an artifact formed by the addition of an additional component during MOF crystallization (Section S.2.2.3, Supporting Information), and points possibly to a homogeneous deposition of NPs onto the outer surface of the nanocrystals already formed at the injection time, that then becomes coated upon subsequent crystal growth. X-ray Photoelectron Spectroscopy (XPS) was used to analyze varying chemical interactions at the resulting MOF-Pt interfaces. All composites show the expected asymmetric 7/2 and 5/2 XPS signal in the Pt 4f region that accounts for the presence of Pt metal with the expected spin-orbit splitting of 3.3 eV (Figure 3b).[20,21] The intensity of these signals for (i) and (e) is gradually less

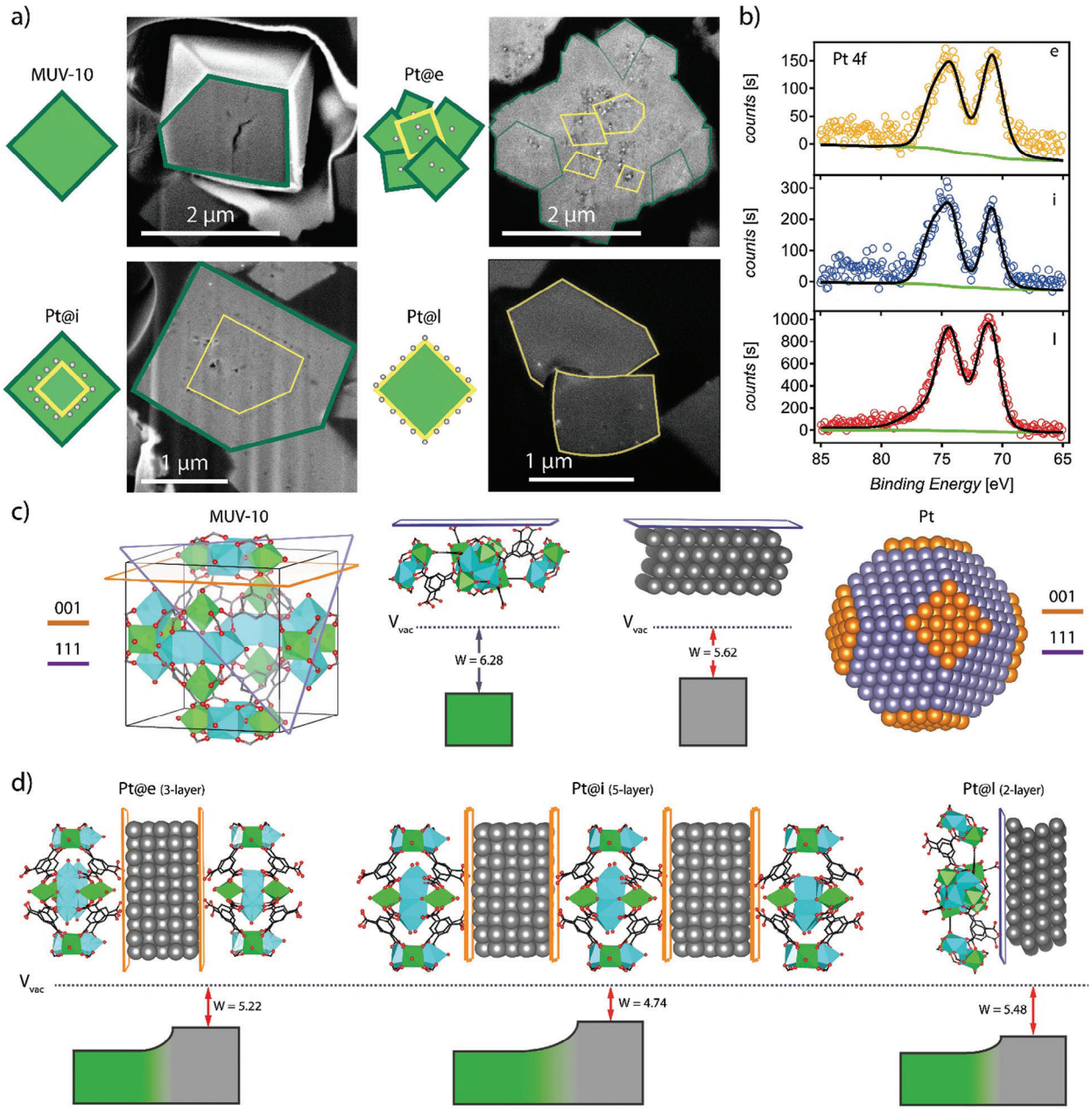

Figure 3. a) FIB-SEM of bare MUV-10 and Pt@MUV-10 showing the integration of Pt in different areas of the crystal as a function of injection time. The diagrams on the left are an idealized representation of the distribution of the nanoparticles (spheres) in the crystal (green) and the corresponding interfaces between them in yellow. The FIB-SEM images are not directly size-comparable as they are sections of the crystals that have been embedded in a polymeric resin. More detailed information on this process can be found in the Supporting Information (Figure S12). b) High-resolution XPS spectra of Pt@MUV-10 indicating the BE for the corresponding Pt 4f 7/2 and 5/2 signals. Note that Pt NPs in the late sample are more accessible than those from the early and intermediate, and thus less peaks are observed when deconvoluted due to the limitation on the sensitivity of the technique. c) Crystallographic planes (001) and (111) in MUV-10 crystals (left) and Pt (right). Work function (*W*) of the (111) surfaces of MUV-10 and Pt relative to the vacuum (center). d) 3, 5, and 2-layer slab models representative of the heterojunctions in MUV-10@Pt composites at early (left), intermediate (middle), and late (right) injection stages. The colors of the planes correspond to the formation of interfaces between either (001) or (111) faces, shown in orange and purple, respectively. The lower panel shows the induced change in the Pt work function for each of the calculated heterojunctions.

intense than for (l), confirming the presence of platinum in the inner sections of these crystals. Pt@MUV-10(e) and (i) also show the same shift toward more electronegative values in their binding energies (BE) of up to 0.3 and 1.8 eV compared to the BE of 71.1 (7/2) and 74.5 eV (5/2) observed for Pt@MUV-10(l), that is closer to the values expected for metallic Pt. Although small, this shift seems to point to a change in Pt bonding or a charge transfer effect between the metal and MOF for these two composites, that is also accompanied by a 0.2 eV shift in the corresponding O1s BE (Figures S14–S16 and Table S6, Supporting Information).

We argued these changes in the electronic hybridization between the MOF and the metal NP could tailor the Pt work function (*W*) for subsequent changes of the built-in electric fields at the corresponding heterojunctions. To explore this possibility, we used Material Studio (MS) 2017 R2 to generate computationally the hypothetical interfaces that could result from Pt injection at varying times. Since MUV-10 and platinum nanocrystals are both cubic, we considered that its integration at the molecular level would occur through equiv. crystallographic faces. The octahedral, sometimes truncated, morphology of MUV-10 crystals is indicative of its thermodynamic preference for the formation of (111) surfaces with a minor contribution of (001) faces.[22] This balance between dominant and secondary crystallographic faces is also present in the surface of 3 nm Pt nanoparticles which would be compatible with the epitaxial integration of both lattices through either (111) or (001) faces. We used slab models to calculate the variation in the work function of both components before (Figure 3c) and after (Figure 3d) the formation of the corresponding heterojunctions. Section S3.1.1 (Supporting Information) contains all methodological details for this analysis. The slab models were adjusted to the early, intermediate, or late stages of Pt injection based on the differences observed in the FIB-SEM analysis of the composites. This analysis reflects either the growth of MUV-10 around the NPs (3-layers, Figure 3d left), an organized encapsulation between alternating crystal faces (5-layers, Figure 3d center), or finally the deposition on the surface of crystals already formed (2-layers, Figure 3d right). Additionally, while in the case of MUV-10(l) Pt incorporation occurs on the dominant (111) faces of the already formed crystal, for cases (e) and (i), where the integration occurs during crystal growth, we opted for the hybridization of both components through the more reactive (001) faces as the best representation of the possible heterojunctions formed. Other combinations of crystallographic faces were also analyzed, and the results are summarized in the Supporting Information (Table S9).

As shown in Figure 3c, the work function values for the isolated surfaces of Pt (111) and MUV-10 (111) are 5.62 eV and 6.28 eV, respectively. When both components are integrated and become in close contact at varying stages of MUV-10 growth, electrons will be transferred from MUV-10 to Pt until the work function at the interface tends to equilibrate (Figure 3d). Compared to the heterojunctions formed by injection at early and late stages of MUV-10 formation for which the decrease of *W* remains equal or below 0.4 eV, the organized distribution of NPs in MUV-10(i) crystal composites doubles this reduction in 0.88 eV for an induced work function of 4.74 eV. It is worth noting that this same effect is also observed for other combinations of crystallographic faces and anticipates more effective charge injection/extraction only for the MUV-10@Pt(i) interfaces upon interfacial adjustment of the work function in this specific composite.

To confirm this effect, we next collected the H_2 production rates of 1 mg mL^{-1} dispersions of Pt@MUV10(e), (i) and (l) in H_2O:CH_3OH (70:30, v:v) under constant irradiation at 100 mW cm^{-2} with a 150 W Xe lamp (**Figure 4a**). We also collected the activity of bare MUV-10 for comparison purposes. Though the incorporation of Pt enhances H_2 generation in all cases, this effect is much more pronounced in Pt@MUV10(i) for a cumulative of 2.58 mmol g^{-1} H_2 after 6 h. This difference is even bigger when all production rates are normalized to the

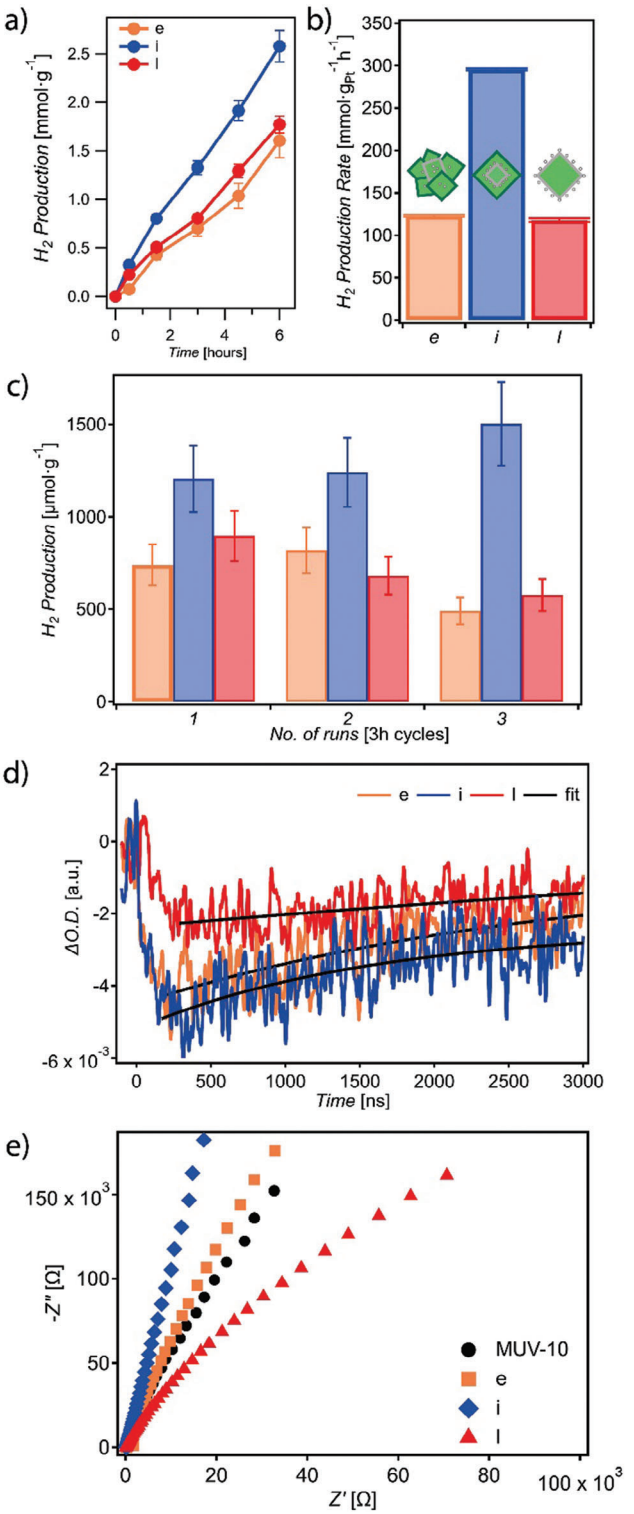

Figure 4. Hydrogen production rates for Pt@MUV-10 composites a) non-normalized and b) normalized to mass of platinum. c) Statistical deviation and cyclability tests. c) TA decay of N_2-saturated dispersions of the samples in MeCN, monitored at 550 nm. $\lambda_{excitation}$ = 300 nm. Black lines correspond to experimental data fitting to single-exponential function. d) Nyquist graph illustrating the impedance changes of the samples over time, consisting with the formation of the electronic interface for the intermediate sample.

amount of Pt present in each composite according to ICP-MS analysis (Figure 4b). While the H_2 production rates of (e) and (l) are practically equal, suggesting a poor electronic integration of Pt with MOF upon addition at early or late stages of crystal formation, this activity is multiplied by 2.4 times in (i). It is interesting to see how the magnitude of this improvement seems to correspond linearly with the induced modification of the Pt work function anticipated for this composite. To confirm this behavior, we repeated the same experiments for all samples in triplicate, and in three consecutive 3-h irradiation cycles (Figure 4c). The results confirm that the boost in activity is unique to Pt@MUV-10(i) and is maintained throughout the cycles compared to the smaller differences observed for (e) and (l). These results suggest that only the injection at an intermediate stage is adequate to access Pt-based heterojunctions with distinctive photocatalytic activity. Based on the results discussed above, this is possibly associated with an organized distribution of NPs in discontinuous sections of the crystal for a more effective electronic hybridization and modification of the metal work function. To further investigate the relationship between this boost in photocatalytic activity and the variations in photo-induced charge recombination, laser transient absorption spectroscopy (L-TAS) experiments were carried out. The TA of Pt@MUV-10(e), (i) and (l) samples have been acquired at 1μs ($\lambda_{Excitation}$ = 300 nm) (Figure S25, Supporting Information). In all cases, a negative, broad band covering the visible range has been obtained, indicating recovery of the ground state (Figure 4d). The TA kinetics have been monitored at 550 nm, and the experimental data fitted to a single-exponential function (Section S4.1.3, Supporting Information). The carrier lifetime of Pt@MUV-10(i) (5.4 μs) is more than 2 times longer than that of (e) and (l) (2.1 and 2.8 μs, respectively), confirming that the injection at an intermediate stage is more efficient in preventing the recombination of photogenerated electron-hole pairs at the MOF/Pt interface. It is worth noticing that differences in carrier lifetime between the samples are consistent with the obtained H_2 evolution values and the calculated Pt work functions, confirming the relationship between the structural and electronic integration achieved with this time-resolved synthetic method. Furthermore, the electronic impedance spectroscopy (EIS) measurements represented in Figure 4d on a Nyquist plot showed variations in the resistive and capacitive behaviors of the Pt@MUV-10, especially for the intermediate sample which variations demonstrate the electronic and ionic properties alignment indicating an effective formation of an electronic MOF-NP interface. More detailed information can be found in the Supporting Information (Section S4).

Supplementary Table S13 summarizes the results obtained by different groups for hydrogen photoevolution using various photocatalytic MOFs with Pt as co-catalyst. According to recent studies,[23] the lack of a standardized methodology makes direct comparison impossible, preventing the normalization of results based on the amount of incorporated Pt or its integration into the MOF under a consistent methodology without variations in the sacrificial agent or irradiation conditions. It is important to emphasize that the focus of this work is not on achieving very high net production values, which in our case might be limited by the intrinsic characteristics of MUV-10, but rather on presenting the controlled integration of the co-catalyst as a new synthetic alternative to engineer performance that is often disregarded. This strategy offers significant versatility as it can be adapted to existing frameworks, nanostructured co-catalysts and photocatalytic reaction types, by leveraging the molecular nature of MOFs to facilitate electronic hybridization of exogenous components in ways that classical semiconductors, such as TiO_2, cannot achieve.

Supporting Information

Supporting Information is available from the Wiley Online Library or from the author.

Acknowledgements

This work was supported by the EU (ERC-2021-COG-101043428 & ERC-2022-POC-101113106), the Generalitat Valenciana (PROMETEU-2021-054 & MFA/2022/026) and the Spanish government (CEX2019-000919-M, PID2023-149922OB-I00 & CNS2022-135677). The authors also thank the SCSIE of the University of València for access to its research facilities.

Conflict of Interest

The authors declare no conflict of interest.

Data Availability Statement

The data that support the findings of this study are available from the corresponding author upon reasonable request.

Keywords

interface, nanoparticle integration, photocatalytic heterojunctions, time-resolved, titanium framework

Received: December 28, 2024
Published online:

[1] R. Freund, S. Canossa, S. M. Cohen, W. Yan, H. Deng, V. Guillerm, M. Eddaoudi, D. G. Madden, D. Fairen-Jimenez, H. Lyu, L. K. Macreadie, Z. Ji, Y. Zhang, B. Wang, F. Haase, C. Wöll, O. Zaremba, J. Andreo, S. Wuttke, C. S. Diercks, *Angew. Chem., Int. Ed.* **2021**, *60*, 23946.
[2] R. Freund, O. Zaremba, G. Arnauts, R. Ameloot, G. Skorupskii, M. Dincă, A. Bavykina, J. Gascon, A. Ejsmont, J. Goscianska, M. Kalmutzki, U. Lächelt, E. Ploetz, C. S. Diercks, S. Wuttke, *Angew. Chem., Int. Ed.* **2021**, *60*, 23975.
[3] A. Dhakshinamoorthy, A. M. Asiri, H. García, *Angew. Chem., Int. Ed.* **2016**, *55*, 5414.
[4] K. Sun, Y. Qian, H. Jiang, *Angew. Chem., Int. Ed.* **2023**, *62*, 202217565.
[5] S. Navalón, A. Dhakshinamoorthy, M. Álvaro, B. Ferrer, H. García, *Chem. Rev.* **2023**, *123*, 445.
[6] T. Devic, C. Serre, *Chem. Soc. Rev.* **2014**, *43*, 6097.
[7] H. Assi, G. Mouchaham, N. Steunou, T. Devic, C. Serre, *Chem. Soc. Rev.* **2017**, *46*, 3431.
[8] a) S. Yuan, J.-S. Qin, H.-Q. Xu, J. Su, D. Rossi, Y. Chen, L. Zhang, C. Lollar, Q. Wang, H.-L. Jiang, D. H. Son, H. Xu, Z. Huang, X. Zou, H.-C. Zhou, *ACS Cent. Sci.* **2018**, *4*, 105; b) S. Wang, T. Kitao, N. Guillou, M. Wahiduzzaman, C. Martineau-Corcos, F. Nouar, A. Tissot, L. Binet, N. Ramsahye, S. Devautour-Vinot, S. Kitagawa, S. Seki, Y. Tsutsui, V.

Briois, N. Steunou, G. Maurin, T. Uemura, C. Serre, *Nat. Commun.* **2018**, *9*, 1660; c) J. Castells-Gil, N. M. Padial, N. Almora-Barrios, J. Albero, A. R. Ruiz-Salvador, J. González-Platas, H. García, C. Martí-Gastaldo, *Angew. Chem., Int. Ed.* **2018**, *57*, 8453; d) N. M. Padial, J. Castells-Gil, N. Almora-Barrios, M. Romero-Angel, I. da Silva, M. Barawi, A. García-Sánchez, V. A. de la, P. O'Shea, C. Martí-Gastaldo, *J. Am. Chem. Soc.* **2019**, *141*, 13124; e) S. Wang, H. Reinsch, N. Heymans, M. Wahiduzzaman, C. Martineau-Corcos, G. D. Weireld, G. Maurin, C. Serre, *Matter.* **2020**, *2*, 440; f) J. Castells-Gil, N. M. Padial, N. Almora-Barrios, R. Gil-San-Millán, M. Romero-Ángel, V. Torres, I. da Silva, B. C. J. Vieira, J. C. Waerenborgh, J. Jagiello, J. A. R. Navarro, S. Tatay, C. Martí-Gastaldo, *Chem.* **2020**, *6*, 3118; g) A. Cadiau, N. Kolobov, S. Srinivasan, M. G. Goesten, H. Haspel, A. V. Bavykina, M. R. Tchalala, P. Maity, A. Goryachev, A. S. Poryvaev, M. Eddaoudi, M. V. Fedin, O. F. Mohammed, J. Gascon, *Angew. Chem., Int. Ed.* **2020**, *59*, 13468; h) S. Wang, M. Cabrero-Antonino, S. Navalón, C. Cao, A. Tissot, I. Dovgaliuk, J. Marrot, C. Martineau-Corcos, L. Yu, H. Wang, W. Shepard, H. García, C. Serre, *Chem.* **2020**, *6*, 3409; i) J. T. Bryant, M. W. Logan, Z. Chen, M. Djokic, D. R. Cairnie, D. A. Vazquez-Molina, A. Nijamudheen, K. R. Langlois, M. J. Markley, G. Pombar, A. A. Holland, J. D. Caranto, J. K. Harper, A. J. Morris, J. L. Mendoza-Cortes, T. Jurca, K. W. Chapman, F. J. Uribe-Romo, *J. Am. Chem. Soc.* **2023**, *145*, 4589; j) N. M. Padial, C. Chinchilla-Garzón, N. Almora-Barrios, J. Castells-Gil, J. González-Platas, S. Tatay, C. Martí-Gastaldo, *J. Am. Chem. Soc.* **2023**, *145*, 21397; k) S.-C. Fan, J.-W. Wang, W. Yuan, P. Zhang, Y. Wang, Q.-G. Zhai, *Chem.* **2024**, *10*, 1804.

[9] N. Kolobov, M. G. Goesten, J. Gascon, *Angew. Chem., Int. Ed.* **2021**, *60*, 26038.

[10] M. Kalaj, K. C. Bentz, S. Ayala, J. M. Palomba, K. S. Barcus, Y. Katayama, S. M. Cohen, *Chem. Rev.* **2020**, *120*, 8267.

[11] A. Chatterjee, L. Wang, P. V. D. Voort, *Chem. Commun.* **2023**, *59*, 3627.

[12] a) J. Wei, X. Mu, Y. Hu, L. Liu, X. Wu, Q. Liu, T. Zhang, Y. Peng, J. Cao, C. Yan, Y. Tang, *Angew. Chem., Int. Ed.* **2023**, *62*, 202302986; b) J. Wei, X. Mu, Y. Hu, L. Liu, X. Wu, Q. Liu, T. Zhang, Y. Peng, J. Cao, C. Yan, Y. Tang, *Angew. Chem.* **2023**, *135*, 202302986.

[13] V. Diez-Cabanes, K. Granados-Tavera, I. Shere, G. Cárdenas-Jirón, G. Maurin, *Chem. Sci.* **2024**, *15*, 15232.

[14] L. Yuan, C. Zhang, Y. Zou, T. Bao, J. Wang, C. Tang, A. Du, C. Yu, C. Liu, *Adv. Funct. Mater.* **2023**, *33*, 2214627.

[15] T. L. Huec, A. López-Francés, I. A. Lázaro, S. Navalón, H. G. Baldoví, M. Giménez-Marqués, *ACS Nano.* **2024**, *18*, 20201.

[16] A. Dhakshinamoorthy, Z. Li, S. Yang, H. Garcia, *Chem. Soc. Rev.* **2024**, *53*, 3002.

[17] C. Fernández-Conde, Y. Zheng, M. Mon, A. Ribera, A. Leyva-Pérez, C. Martí-Gastaldo, *Chem. Sci.* **2024**, *15*, 2351.

[18] B. Lerma-Berlanga, C. R. Ganivet, N. Almora-Barrios, S. Tatay, Y. Peng, J. Albero, O. Fabelo, J. González-Platas, H. García, N. M. Padial, C. Martí-Gastaldo, *J. Am. Chem. Soc.* **2021**, *143*, 1798.

[19] A. Centrone, B. Lerma-Berlanga, A. J. Biacchi, C. Fernández-Conde, G. Pavlidis, C. Marti-Gastaldo, *Adv. Funct. Mater.* **2023**, *33*, 2302357.

[20] H. Khajavi, H. A. Stil, H. P. C. E. Kuipers, J. Gascon, F. Kapteijn, *ACS Catal.* **2013**, *3*, 2617.

[21] K. Kratzl, T. Kratky, S. Günther, O. Tomanec, R. Zbořil, J. Michalička, J. M. Macak, M. Cokoja, R. A. Fischer, *J. Am. Chem. Soc.* **2019**, *141*, 13962.

[22] N. M. Padial, B. Lerma-Berlanga, N. Almora-Barrios, J. Castells-Gil, I. da Silva, M. de la Mata, S. I. Molina, J. Hernández-Saz, A. E. Platero-Prats, S. Tatay, C. Martı´-Gastaldo, *J. Am. Chem. Soc.* **2020**, *142*, 6638.

[23] L. Yao, A. M. Pütz, H. Vignolo-González, B. V. Lotsch, *J. Am. Chem. Soc.* **2024**, *146*, 9479.

